ACS APPLIED MATERIALS & INTERFACES

Research Article

Regulation of Osteoblast Proliferation and Differentiation by Interrod Spacing of Sr-HA Nanorods on Microporous Titania Coatings

Jianhong Zhou,[†] Bo Li,[†] Shemin Lu,[‡] Lan Zhang,[†] and Yong Han*,[†]

[†]State Key Laboratory for Mechanical Behavior of Materials, Xi'an Jiaotong University, Xi'an 710049, China

[‡]Department of Genetics and Molecular Biology, College of Medicine, Xi'an Jiaotong University, Xi'an 710061, China

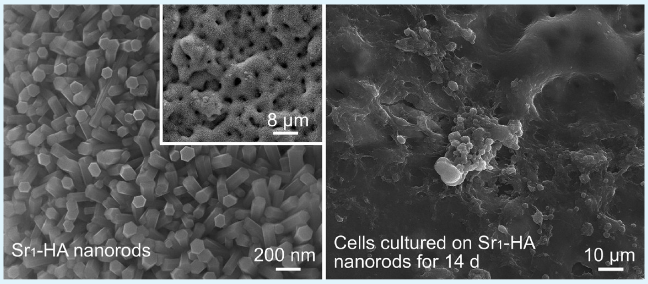

ABSTRACT: Strontium-doped hydroxyapatite ($Ca_9Sr_1(PO_4)_6(OH)_2$, Sr_1-HA) nanorods with different lateral spacing (e.g., interrod spacing) values (67.3 ± 3.8, 95.7 ± 4.2, and 136.8 ± 8.7 nm) and nanogranulates were grown on microarc-oxidized microporous TiO_2, respectively, to form multilayer coatings. The coatings reveal two kinds of micro/nanoscaled hierarchical surfaces with a similar microscale roughness, e.g., nanogranulated 2D pattern and nanorod-shaped 3D pattern in nanotopography. When hFOB1.19 cells are employed, the proliferation and differentiation of osteoblasts on the coatings were evaluated by examining MTT assay, expressions of osteogenesis-related genes [alkaline phosphatase (ALP), runt-related transcription factor 2, osterix, osteopontin (OPN), osteocalcin (OCN), and collagen I (Col-I)], ALP activity, contents of intracellular Ca^{2+}, Col-I, OPN, and OCN, extracellular collagen secretion, and extracellular matrix mineralization. The results reveal that the proliferation and differentiation of osteoblasts can be directly regulated by the interrod spacing of the Sr_1-HA nanorods, which are significantly enhanced on the nanorod-shaped 3D patterns with interrod spacing smaller than 96 nm and more pronounced with decreasing the interrod spacing but inhibited on the nanorods with spacing larger than 96 nm compared to the nanogranulated 2D pattern. The difference in the cellular activity is found to be related with the intracellular Ca^{2+} concentrations, which are regulated by variation of the surface topology of Sr_1-HA crystals. Our work provides insight to the surface structural design of a biomedical implant favoring osteointegration.

KEYWORDS: *Sr-doped hydroxyapatite, nanorod, interrod spacing, osteoblast, proliferation, differentiation*

1. INTRODUCTION

An important aspect of orthopedic implant integration is enhancement of the functional activity of osteoblasts at the tissue−implant interface without any fibrous tissue intervention.[1] Current orthopedic implants are limited by the lack of appropriate cell−material interactions and osteointegration, leading to a reduced implant lifespan.[2] Cell−material interactions play a key role in the healing of wound bone, which dependd on the specific surface properties of the material such as chemistry,[3−6] surface energy/wettability,[3,7] roughness,[8,9] and topography.[10−15] Recent works demonstrated that three-dimensional (3D) nanotopography of materials could separately influence the cell proliferation and differentiation, independent of the surface chemistry and wettability; however, conflicting results have been reported. For example, quasi-aligned TiC and TiO_2 nanowires,[10] hydroxyapatite (HA) nanoneedles, and nanofibers[11] inhibited the cell proliferation and differentiation. By contrast, upright silicon nanowires[12] and ordered/disordered fluorapatite nanorods[13] improved the cell differentiation but inhibited the proliferation; the other lines revealed that ZnO nanoflowers,[14] gold-coated silicon nanopillars,[15] improved the proliferation and differentiation of cells compared to the corresponding two-dimensional (2D) counterparts. On the other hand, studies on the chemical composition of nanoscale substrate topographies have also highlighted the significance of HA in controlling the cellular response.[16,17] Moreover, strontium-doped HA ($Ca_{10-x}Sr_x(PO_4)_6(OH)_2$, Sr_x-HA) with a Sr dose lower than 20 atom % enhanced the osteoblast activity and the positive effect of HA on bone regeneration.[18,19] Therefore, it is necessary to construct the nanopatterned surface of an implant favoring positive interaction with osteoblasts.

Hydrothermal treatment (HT) has been shown to be an effective way to create HA-grade (such as HA, fluoridated/carbonated HA, and Sr_x-HA) nanorods and nanofibers. However, these HA-grade products are mostly in the form of powders rather than films/coatings. For hydrothermally formed HA films, Chen et al. have reported that a film of compacted fluoridated HA nanorods was grown on metal plates;[20] recent works have just shown compacted layers of micrometer-sized

Received: April 12, 2013
Accepted: May 13, 2013
Published: May 13, 2013

equiaxed HA crystals on Ti6Al4 V substrates[21] or polygonal-shaped HA nanoparticles on a titanium−niobium alloy substrate.[22] Since Ishizawa et al. first applied a hybrid approach of microarc oxidation (MAO) and HT to titanium and its alloy,[23] there has been no significant progress in morphology and size control of the HA crystals, although great efforts have been made; the HA crystals formed via the hybrid approach in all of the published literature not only have been submicrometer-sized short rodlike but have also a wide lateral spacing between rods (more than several hundred nanometers to several micrometers), as revealed in the representative works.[23−25]

In our previous works, we reported a one-step method of MAO to form HA/$CaTiO_3$/TiO_2-$CaTiO_3$ and Sr_{10}-HA/$SrTiO_3$/$SrTiO_3$-TiO_2 coatings with outerlayers to be nanogranulated,[26,27] which also synthesized Sr_1-HA/$Ca_{0.5}Sr_{0.5}TiO_3$/TiO_2 coatings with outerlayers to be nanofiberous or nanorod-shaped using a two-step method of MAO and HT,[28] and revealed that the multilayer coatings could firmly adhere to titanium substrates. An in-depth understanding of the cell activity of such fibrous/rod-shaped and granulated non-otopographies would have considerable scientific importance for the nanopattern design of an implant surface favoring positive osseointegration. In the present study, Sr_1-HA nanorods with different lateral spacing were hydrothermally grown on microarc-oxidized microporous TiO_2, and the proliferation and differentiation of osteoblasts on the 3D Sr_1-HA nanorod-patterned surfaces were investigated together with 2D Sr_1-HA nanogranule-patterned surfaces to identify the effect of such nanopatterns on the cell function.

2. EXPERIMENTAL SECTION

2.1. Preparation of Sr_1-HA Nanogranule/Rod-Patterned Multilayer Coatings. Commercial pure titanium disks with sizes of ⌀ 15 × 2 mm were employed as substrates. For the formation of a Sr_1-HA nanogranule-patterned multilayer coating by a one-step method of MAO, as described in detail elsewhere,[26,27] titanium disks were used as anodes and treated using a pulse power supply in an aqueous electrolyte containing 0.167 M calcium acetate (CA), 0.033 M strontium acetate (SA), and 0.02 M β-glycerophosphate disodium (β-GP) at an applied voltage of 480 V, a pulse frequency of 100 Hz, and a duty ratio of 26% for 5 min. For the formation of Sr_1-HA nanorod-patterned multilayer coatings, as described in detail elsewhere,[28] the titanium disks were first treated by MAO using a bipolar pulse power supply in an aqueous electrolyte containing different concentrations of CA, SA, and β-GP at an applied positive pulse voltage of 380 V, a negative pulse voltage of 100 V, a pulse frequency of 100 Hz, and a duty ratio of 26% for 5 min; then the microarc-oxidized coatings were mounted in a Teflon-lined autoclave containing distilled water with an initial pH value of 6.4 to receive HT at 140 °C for 24 h. The hydrothermally treated microarc-oxidized coatings were marked in Table 1.

2.2. Structural Characterization of the Multilayer Coatings. Phase identification was carried out by an X-ray diffractometer (X'Pert Pro, The Netherlands) in θ−2θ geometry using Cu Kα (λ = 0.15406 nm) radiation over a 2θ angle of 20−80° at a step of 0.017°. The morphologies of the coatings were examined by field-emission scanning electron microscopy (FESEM; JEOL JSM-6700F, Japan). The nanorods scratched from the coating surfaces were examined by transmission electron microscopy (TEM; JEOL JEM-2000FX, Japan) operating at 200 kV. The roughness of the coatings was examined by atomic force microscopy (AFM; SPM-9500J3, Japan). The hydrophilicity of the coatings was measured by a surface contact-angle measurement machine (DSA30, Kruss, Germany).

Table 1. Hydrothermally Treated Microarc-Oxidized Coatings and the Corresponding Used Electrolyte Compositions for MAO

	aqueous electrolyte compositions (M)		
coating	CA	SA	β-GP
S67	0.167	0.033	0.02
S96	0.125	0.025	0.015
S137	0.083	0.017	0.01

2.3. Cell Proliferation Assessment and Morphology Observation. A human fetal osteoblast cell line, hFOB1.19, was purchased from the Insitute of Biochemistry and Cell Biology of Chinese Academy of Sciences (Shanghai, China). The cells were inoculated into Dulbecco's modified Eagle medium supplemented with 10% fetal bovine serum, 0.3 mg/mL Geneticine418 (Sigma, USA), 0.5 mM sodium pyruvate (Sigma, USA), and 1.2 g/L Na_2CO_3 and incubated in a humidified atmosphere incubator with 5% CO_2 and 95% air at 37 °C. The complete medium was refreshed every 2 days.

The samples were placed centrally in 24-well plates with well diameters of 15 mm. hFOB1.19 cells were seeded on each sample at a density of 4×10^4 cells/cm^2 and incubated for 3, 7, and 14 days. At the end of each time period, the complete medium was removed from each well, and the samples were washed three times with phosphate buffered saline (PBS) and then transferred to new 24-well plates. A total 30 μL of a MTT (Sigma, USA) solution (5 mg/mL MTT in PBS) with a 500 μL culture medium was added to each well with continuous culture for 4 h. After removal of the culture medium, 200 μL of dimethyl sulfoxide (DMSO; Sigma, USA) was added into each well and oscillated for 10 min. Finally, 100 μL of DMSO solution from each well was transferred to a 96-well plate, and the absorbance was measured at 490 nm. Four specimens for each group were tested, and each test was repeated four times (n = 4).

After 3 and 14 days of culture, the cell-adhered samples were washed three times with PBS and fixed with 2.5% glutaraldehyde for 1 h at 4 °C. The cell-fixed samples were then dehydrated in ethanol, followed by vacuum drying. After coating gold, the samples were observed under FESEM for cell morphology. The element contents of the cell-adhered coatings were detected by energy-dispersive X-ray spectrometry (EDS).

2.4. Osteogenesis-Related Gene Expressions. The total RNA was isolated using the TRIzol reagent (Gibco, USA). A total of 1 μg of RNA from the cells on each sample was reversed transcribed into complementary DNA using a PrimeScrip RT reagent kit (TaKaRa, Japan). Expressions of osteogenesis-related genes, including the runt-related transcription factor 2 (Runx2), osterix, alkaline phosphatase (ALP), osteopontin (OPN), osteocalcin (OCN), and collagen I (Col-I), were quantified using a real-time polymerase chain reaction (PCR) detection system (Bio-Rad iQ5 Multicolor) with SYBRPremix ExTaqII (TaKaRa, Japan). Data analysis was carried out using a iQ5 Optical System (Bio-Rad, USA) with software version 2.0. The housekeeping gene, glyceraldehyde-3-phosphate dehydrogenase, was used as an endogenous reference gene to normalize calculation through the Comparative Ct value method. The sequence of the specific primer sets is listed as follows: Runx2 (5′-CCTTCTGGGTTCCCGAGGT-3′ and 5′-AGTGGACGAGGCAAGAGTTTC-3′), osterix (5′-TGCGAAGCCTTGCCATACA-3′ and 5′-TCCTCCTGCGACTGCCCTAA-3′), ALP (5′-ATCTTTGGTCTGGCCCCCATG-3′ and 5′-ATGCAGGCTGCATACGCCAT-3′), OPN (5′-ATGGCTTTCGTTGGACTTACT-3′ and 5′-TTTACAACAAATACCCAGATGC-3′), OCN (5′-TCCTGAAAGCCGATGTGGT-3′ and 5′-AGGGCAGCGAGGTAGTGAA-3′), and Col-I (5′-GAAGTCAGCTGCATACAC-3′ and 5′-AGGAAGTCCAGGCTGTCC-3′).

2.5. Intracellular ALP Activity, Specific Proteins, and Col-I Contents as Well as Calcium Ion Concentration. After 3, 7, and 14 days of culture, the cell-seeded samples were washed three times with PBS, transferred to new cell culture plates, then lysed in 0.1 vol % Triton X-100 through five standard freeze−thaw cycles, and shaken for 10 min. The intracellular ALP activity and contents of specific proteins (such as OPN and OCN) and Col-I were determined with respective

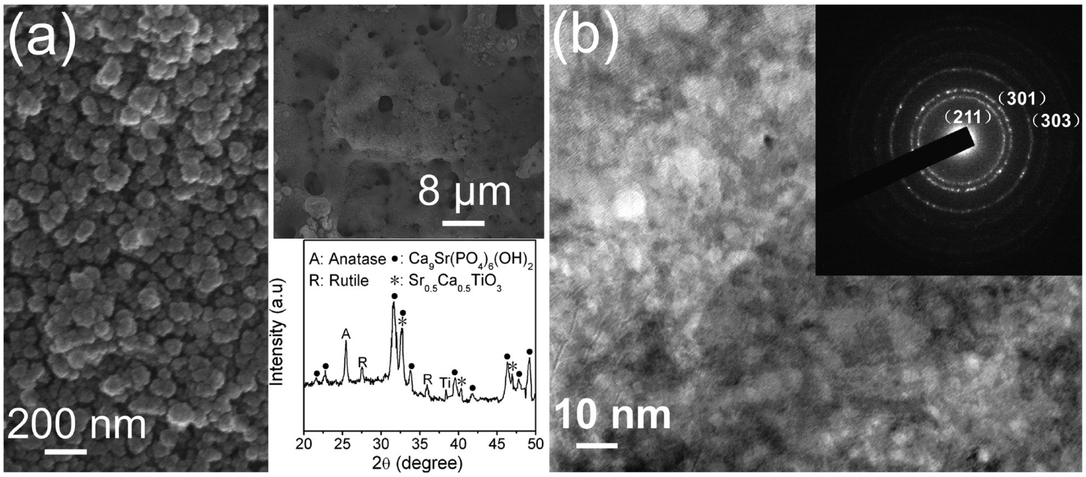

Figure 1. Structure of the coating microarc-oxidized at 480 V: (a) SEM magnified image (top inset showing the low-magnification image and bottom inset showing the XRD pattern); (b) TEM image of the coating surface (inset showing the SAED pattern).

human ELISA kits (R&D, USA). The optical absorbance at 450 nm was recorded spectrophotometrically, and the intracellular ALP activity, specific protein contents, and Col-I amount of osteoblasts cultured on the samples were drawn from a standard curve of absorbance versus known standards of corresponding proteins run in parallel with the experimental samples. The results were normalized to the intracellular total protein content. The intracellular calcium ion (Ca^{2+}) concentration was determined using a calcium assay kit (R&D, USA) according to the manufacturer's instructions. The absorbance was measured at 450 nm, and the Ca^{2+} concentration was calculated using the standard provided in the kit. The result was normalized to cell numbers. Four samples for each group were tested, and each test was repeated four times ($n = 4$).

2.6. Collagen Secretion of Osteoblast and Extracellular Matrix (ECM) Mineralization. Collagen secretion by osteoblasts on the samples was quantified by Sirius Red staining as follows. After 3, 7, and 14 days of culture, the cell-seeded samples were fixed in 4% paraformaldehyde. The samples were stained for collagen secretion in a saturated picric acid solution containing 0.1% Sirius Red (Sigma, USA) for 18 h. In the quantitative analysis, the stain on the samples in which osteoblasts were cultured for 3, 7, and 14 days was eluted in 500 mL of a destain solution (0.2 M 1:1 NaOH/methanol). The optical density at 540 nm was then measured using a spectrophotometer.

ECM mineralization of osteoblasts was analyzed using Alizarin Red staining. The samples, cultured cells for 3, 7, and 14 days, were fixed in 75% ethanol for 1 h and subsequently stained with a 2% Alizarin Red (Sigma, USA) solution for 10 min. Afterward, the samples were washed with distilled water until no color appeared in the distilled water. The images of ECM mineralization were taken at day 14 of the culture. In quantitative analysis, the stain on the samples in which osteoblasts were cultured for 3, 7, and 14 days was dissolved in a 10 mM sodium phosphate aqueous solution containing cetylpyridinum chloride with a volume concentration of 10%, and the absorbance values were measured at 620 nm.

2.7. Statistical Analysis. The data were analyzed using *SPSS 14.0* software (SPSS, USA). A two-way ANOVA followed by a Student−Newman−Keuls posthoc test was used to determine the level of significance. $p < 0.05$ was considered to be significant, and $p < 0.01$ was considered to be highly significant.

3. RESULTS AND DISCUSSION

3.1. Characterization of Sr_1-HA Nanogranulate/Nanorod-Patterned Coatings.

The coating formed by a one-step method of MAO at 480 V is microporous, with an average diameter of 3−4 μm for the pores that distribute homogeneously over the coating (top inset in Figure 1a). The micropores' walls are in the form of compacted nanogranules (Figure 1a). X-ray diffraction (XRD) pattern (bottom inset in Figure 1a) reveals that the coating consists of anatase and rutile TiO_2, $CaSrTiO_3$, and $Ca_9Sr_1(PO_4)_6(OH)_2$ (Sr_1-HA), while TEM observation on the coating surface further confirms that the outermost layer of the coating is solely composed of compacted Sr_1-HA nanogranules, as identified by a selected-area electron diffraction (SAED) pattern (Figure 1b). It is indicated that the coating, named as NG, formed by MAO at 480 V is multilayered by Sr_1-HA as an outer layer with a nanogranulated 2D surface topography and TiO_2-$CaSrTiO_3$ as an inner layer adjacent to the titanium substrate.

Parts a−c of Figure 2 show the SEM surface morphologies of the coatings, named as S67, S96, and S137, formed by MAO and subsequent HT. It is clear that the coatings are also microporous, and the micropores' walls are in the form of nanorods with a similar mean diameter of 70 nm. However, the interrod spacing values of the coatings increase with decreasing

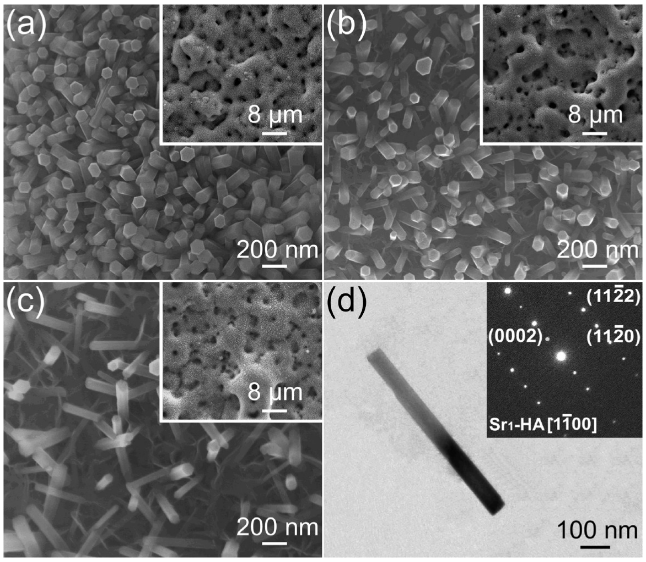

Figure 2. SEM surface morphologies of the microarc-oxidized and hydrothermally treated coatings: (a) S67, (b) S96, and (c) S137 (insets showing the corresponding low-magnification images). (d) TEM bright-field image of the scratched nanorod from the S137 coating (inset showing the SAED pattern).

Table 2. Basic Characteristics of Sr_1-HA Nanorods, Roughness Values, and Contact Angles of the Coatings

			roughness (nm)			
coating	nanorod spacing (nm)	nanorod diameter (nm)	Ra	RMS	Rz	contact angle (deg)
NG			465.4 ± 35.3	495.5 ± 43.7	1235.4 ± 143.7	46.8 ± 5.7
S67	67.3 ± 3.8	71.4 ± 5.6	431.6 ± 43.1	453.9 ± 33.9	1189.8 ± 149.4	4.3 ± 1.5
S96	95.7 ± 4.2	68.9 ± 7.9	437.7 ± 31.3	476.4 ± 46.4	1213.9 ± 172.9	14.5 ± 2.9
S137	136.8 ± 8.7	67.6 ± 5.4	429.6 ± 41.5	485.8 ± 39.3	1185.6 ± 158.4	25.2 ± 3.1

electrolyte concentrations during MAO, which are 67.3 ± 3.8, 95.7 ± 4.2, and 136.8 ± 8.7 nm for the S67, S96, and S137 coatings, respectively (Table 2). As an example, TEM analysis of the scratched individual nanorod from the S137 coating confirms that the nanorods on the coatings are of well-crystallized Sr_1-HA, as identified by the SAED pattern (inset in Figure 2d). The coatings are multilayered, composed of Sr_1-HA as an outer layer with a nanorod-shaped 3D surface topography, $Ca_{0.5}Sr_{0.5}TiO_3$ as a middle layer, and TiO_2 as an inner layer adjacent to the titanium substrate, as described in detail in our previous work, together with their formation mechanism.[28]

The roughness values of the S67, S96, and S137 coatings measured by AFM are listed in Table 2, together with the NG coating. There are no significant differences in the microscale roughness among the coatings, as characterized by the average roughness (Ra), root-mean-square roughness (RMS), and selection of 10-point height of irregularity roughness (Rz). The contact angles of the water droplets on the NG coating as well as the S67, S96, and S137 coatings are 46.8 ± 5.7, 4.3 ± 1.5, 14.5 ± 2.9, and 25.2 ± 3.1°, respectively (Table 2), indicating that the nanorod-patterned coatings can improve the hydrophilicity compared to the nanogranulated coating, and the improvement is more significant with decreasing interrod spacing.

3.2. Cell Proliferation on Nanogranulated and Nanorod-Patterned Coatings.

Figure 3a shows the numbers of osteoblasts on the NG and nanorod-patterned coatings after incubation for 3, 7, and 14 days. They tend to increase with prolonged incubation time for each kind of coating, indicating that cell proliferation occurred since day 3. At each time point, there is an obvious difference in proliferation of cells on the coatings. The S67 and S96 (especially S67) coatings show significant increase in proliferation of cells compared to the NG coating; however, proliferation of cells on the S137 coating is statistically lower than that on the NG coating. Figure 3b shows the morphologies of cells on the coatings after 3 days of incubation. The cells attach and spread more well on the S67 and S96 coatings compared to the NG coating, even almost completely cover the S67 surface. There are many dense lamellipodia and filopodia stretching out to anchor to the S67 and S96 surfaces, forming good intercellular connection, and enhancing cell−cell communication, which can coordinate cellular responses to external signals and regulate osteoblast differentiation.[29,30] In contrast, only a fewer and smaller cells are observed on the S137 coating compared to the NG coating, indicating that the cells cannot grow well on the S137 coating.

Because osteoblast proliferation is marked by the induction of an ECM composed of collagen and noncollagenous proteins,[8] collagen secreted by osteoblasts into ECM was determined at days 3, 7, and 14, as shown in Figure 3c. The detected collagen at day 3 indicates that hFOB1.19 cells on all of the studied coatings are capable of forming ECM at early times of less than 3 days. Furthermore, at each incubation time, the S67 and S96 (especially S67) coatings induce much more collagen secretion compared to the NG coating, while the content of the secreted collagen on the S137 coating is lower than that on the NG coating. The results of Figure 3 suggest that the Sr_1-HA nanorod-patterned 3D topography with interrod spacing smaller than 96 nm promote and that with interrod spacing larger than 96 nm inhibit cell proliferation and ECM synthesis, compared to the nanogranulated 2D topography.

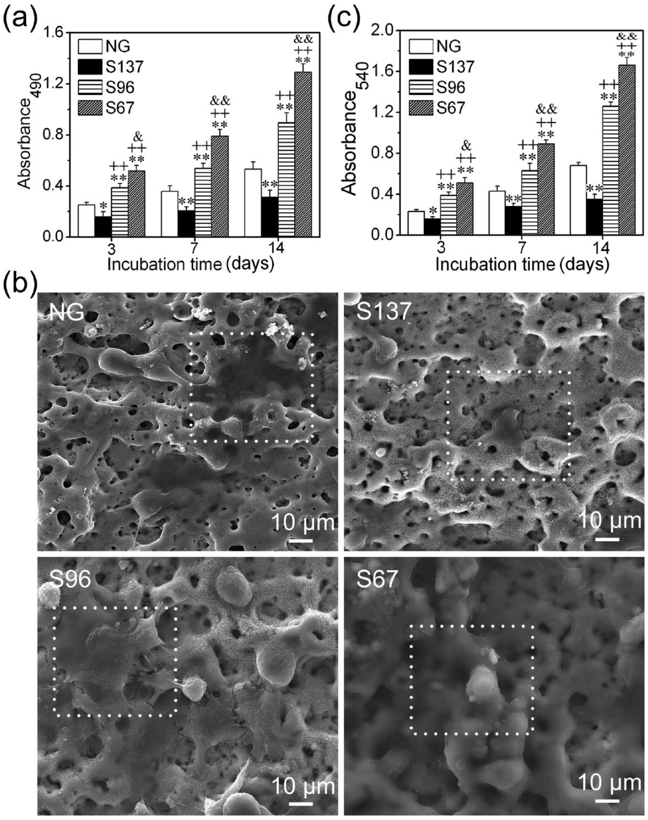

Figure 3. (a) Cell proliferation after 3, 7, and 14 days of incubation measured by MTT assay, (b) morphologies of the osteoblasts cultured on the coatings for 3 days, and (c) collagen secretion on the coatings at 3, 7, and 14 days of incubation. Data are presented as the mean ± SD, $n = 4$, (*) $p < 0.05$ and (**) $p < 0.01$ compared with the NG coating, (++) $p < 0.01$ compared with the S137 coating, and (&) $p < 0.05$ and (&&) $p < 0.01$ compared with the S96 coating.

3.3. Cell Differentiation on Nanogranulated and Nanorod-Patterned Coatings.

Growth and differentiation of osteoblasts can be divided into three main periods: proliferation, during which cells initiate ECM synthesis, ECM maturation, and mineralization,[8,31,32] with peak mRNA levels defining the transition between periods. The differentiation process of hFOB1.19 cells on the coatings can be determined in terms of (1) mRNA expressions of Runx2, osterix, ALP, OPN, OCN, and Col-I and (2) intracellular ALP activity and specific protein (OPN and OCN) and Col-I contents.

Expressions of osteogenesis-related genes, including Runx2, osterix, ALP, OPN, OCN, and Col-I, in cells cultured on coatings for 3, 7, and 14 days were detected, as shown in Figure 4. The mRNA expressions of Runx2, osterix, OCN, and Col-I in the cells cultured on the coatings increase with incubation time from 3 to 14 days. The difference among them is that the mRNA levels of OCN are very low at day 3, while Runx2, osterix, and Col-I show up-regulated expressions at day 3. At each incubation time, it is worth noticing that the expressions of Runx2, osterix, OCN, and Col-I mRNA in the cells are significantly higher on the S67 and S96 (especially S67) coatings but significantly lower on the S137 coating compared to the NG coating. A similar variation trend is observed for the expression levels of the ALP and OPN genes on the coatings with increasing incubation time from 3 to 7 days. At day 14, ALP and OPN mRNA expressions on the S167 and NG coatings are significantly increased but obviously down-regulated by the S67 and S96 coatings compared to those at day 7.

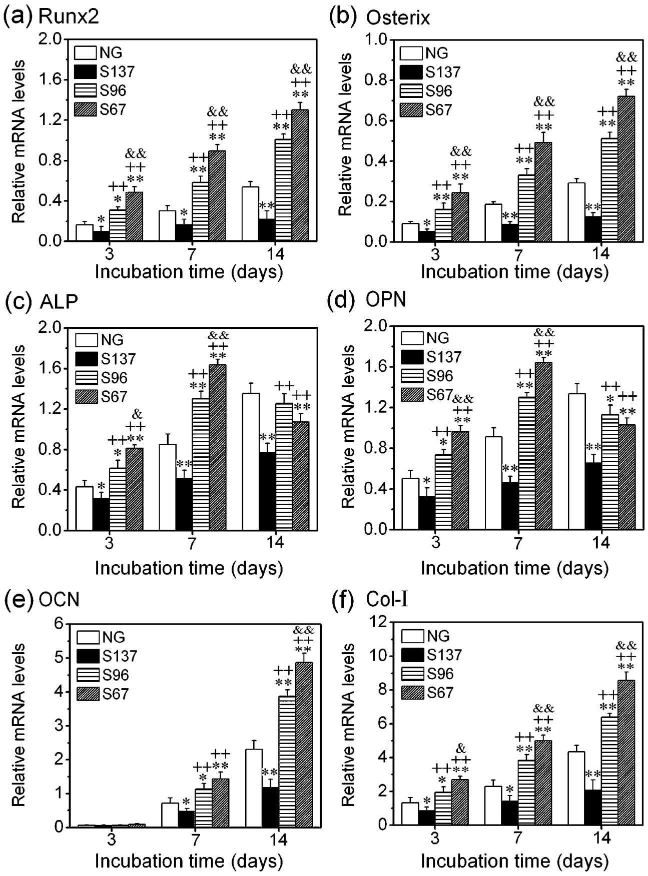

Figure 4. Gene expressions of osteoblasts cultured on the NG, S137, S96, and S67 coatings after incubation of 3, 7, and 14 days: (a) Runx2; (b) osterix; (c) ALP; (d) OPN; (e) OCN; (f) Col-I. Data are presented as the mean ± SD, $n = 4$, (*) $p < 0.05$ and (**) $p < 0.01$ compared with the NG coating, (++) $p < 0.01$ compared with the S137 coating, and (&) $p < 0.05$ and (&&) $p < 0.01$ compared with the S96 coating.

Figure 5 reveals intracellular ALP activity and contents of specific proteins (OPN and OCN) and Col-I in the cells cultured on the coatings for 3, 7, and 14 days. The variation trend of intracellular ALP activity as well as OCN and Col-I contents with culture time is similar to that of their corresponding gene expressions in the cells on the coatings. However, the S67 and S96 coatings show significantly higher intracellular OPN contents at day 14 compared to day 7, which is different from the trend of OPN mRNA expressions at these two time points. This might be due to delayed variation in the protein lever of OPN relative to its mRNA level with culture time because protein is a downstream product of the gene. These results reveal that the intracellular protein synthesis can be significantly enhanced on the S67 and S96 coatings but inhibited on the S137 coating compared to the NG coating.

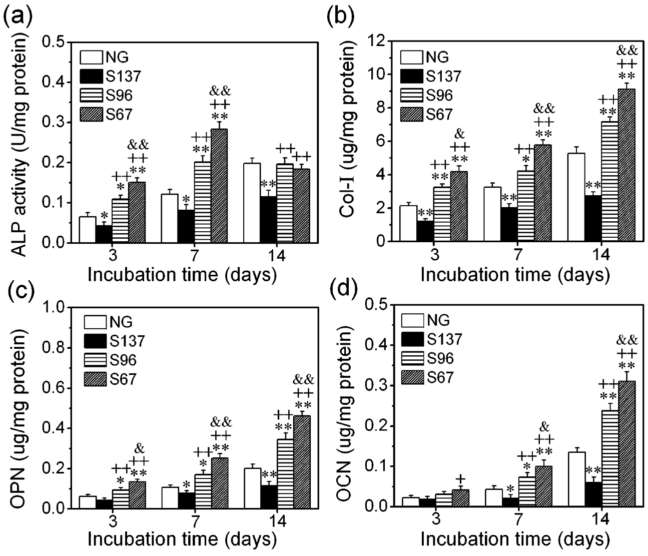

Figure 5. (a) ALP activity as well as contents of (b) Col-I, (c) OPN, and (d) OCN proteins in osteoblasts cultured on the NG, S137, S96, and S67 coatings for 3, 7, and 14 days. Data are presented as the mean ± SD, $n = 4$, (*) $p < 0.05$ and (**) $p < 0.01$ compared with the NG coating, (+) $p < 0.05$ and (++) $p < 0.01$ compared with the S137 coating, and (&) $p < 0.05$ and (&&) $p < 0.01$ compared with the S96 coating.

ECM mineralization on the coatings after 3, 7, and 14 days of incubation, determined with Alizarin Red staining, is shown in Figure 6. According to the quantitative colorimetrical figure in Figure 6a, at each culture time ECM mineralization is significantly promoted on the S67 and S96 (especially S67) coatings but inhibited on the S137 coating compared to the NG coating. Staining pictures of ECM mineralization (Figure 6b) taken at day 14 give visual evidence to support this conclusion. Figure 6c shows the SEM morphologies of the cells on the coatings after 14 days of incubation. Compared with those at 3 days shown in Figure 3b, the cells cultured on the S67 and S96 coatings for 14 days exhibit more mineral particles on the cells' surfaces than the NG coating, which are rich in calcium, phosphorus, and carbon, as shown in Table 3. However, almost no mineral particles can be observed by SEM and detected by EDS on the surfaces of cells cultured on the S137 coating.

As is known, Runx2 is a transcription factor necessary for early osteoblast differentiation,[33] while osterix is a zinc finger transcription factor specifically expressed by osteoblasts to induce differentiation of osteoblast to a mature phenotype.[34] ALP is a key marker of osteoblast differentiation in vitro, with peak mRNA and activity levels pronouncing osteoblast maturation, and the levels then decrease at the onset of mineralization.[35] OPN is a middle-stage maker of osteogenic differentiation, at later time points, associated with the onset of ECM mineralization, achieving a peak level of gene expression

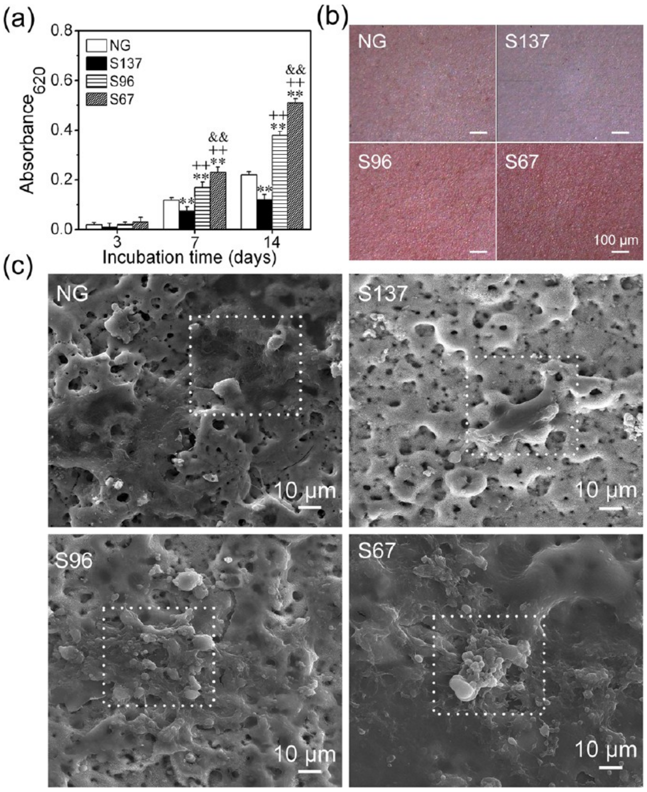

Figure 6. ECM mineralization of osteoblasts on the coatings determined with Alizarin Red staining and cell morphologies: (a) colorimetrically quantitative analysis at 3, 7, and 14 days of incubation; (b) staining pictures of ECM mineralization at 14 days of incubation. (c) SEM morphologies of the osteoblasts cultured on the coatings for 14 days. Data are presented as the mean ± SD, $n = 4$, (**) $p < 0.01$ compared with the NG coating, (++) $p < 0.01$ compared with the S137 coating, and (&&) $p < 0.01$ compared with the S96 coating.

paralleling the accumulation of mineral.[9] OCN is a late-stage maker of osteoblast differentiation,[36] and its production denotes the onset of ECM deposition.[35] Col-I is the most abundant bone matrix protein and can induce osteoblastic differentiation.[37] The enhanced Runx2, osterix, and ALP mRNA expressions as well as ALP activities on the S67 and S96 coatings compared to the NG coating at days 3 and 7, in this work, indicate that these 3D nanopatterns with interrod spacing smaller than 96 nm accelerate the differentiation by promoting maturation of the cells at an earlier time compared to the 2D nanopattern. Most notably, the decrease in ALP caused by the S67 coating at both mRNA and activity levels following day 7 further suggests that this 3D nanopattern accelerates ECM mineralization, and the cell differentiation on this pattern progresses into the ECM mineralization period at day 7. Moreover, a peak level of the OPN mRNA expression on the S67 coating at day 7 (Figure 4d) also indicates that the coating can promote the cells progressing into the ECM mineralization period at an earlier time compared to the other coatings. In the ordered sequence of events occurring during osteoblast differentiation, the increase of the ALP activity is followed by increased synthesis of Col-I and then finally deposition of the noncollagenous ECM proteins, such as OPN and OCN, to form bone.[35] Our results reveal that compared to the NG coating, the S67 and S96 coatings not only remarkably enhance the expression of OCN and Col-I mRNA but also significantly promote the production of intracellular OPN, OCN, and Col-I at 3, 7, and 14 days. The increase in the contents of intracellular OPN and OCN caused by the S67 and S96 coatings would lead to more of these proteins to secrete into ECM, and therefore the accelerated mineralization of ECM is expected, as supported by Figure 6. Synergistically taking into consideration the opposite response of cells to the S137 coating compared to the NG coating, it is highlighted that the 3D nanopatterns with interrod spacing smaller than 96 nm accelerate differentiation of the hFOB1.19 cells, not only promoting the cells to a mature phenotype but also expediting ECM mineralization at an earlier time; however, the 3D nanopatterns with interrod spacing larger than 96 nm inhibit the cells to a mature phenotype and ECM mineralization compared to the 2D nanopattern.

With regard to the orthopedic implants, the most important issue is to balance the dilemma between cell proliferation and differentiation and to enhance both of them simultaneously. It has been reported that upright silicon nanowires and ordered/disordered fluorapatite nanorod-patterned surfaces are effective in promoting osteoblast differentiation but depress osteoblast proliferation,[12,13] which could lead to less cell colonization on them and, accordingly, result in smaller bone mass around them compared with relatively smooth 2D patterned surfaces.[38,39] Different from the above-mentioned osteoblast response, our results demonstrate that the Sr_1-HA nanorod-shaped 3D patterns with interrod spacing smaller than 96 nm can simultaneously significantly accelerate the proliferation, differentiation, and mineralization of hFOB1.19 cells compared to the Sr_1-HA nanogranulated 2D pattern; furthermore, the accelerating effect is more significant with narrowing of the interrod spacing. However, the nanorod-shaped 3D patterns

Table 3. Element Contents Detected by EDS in the Square Marked on the Cells Shown in Figures 3b and 6c, Together with the Difference in the Element Contents of Calcium and Phosphorus between 14 and 3 days of Incubation

		element contents (atom %)						difference in the element contents	
coatings	incubation time (days)	Ti	C	O	Ca	P	Sr	ΔCa	ΔP
NG	3	14.1 ± 0.6	12.9 ± 0.9	59.9 ± 3.6	6.1 ± 0.6	4.7 ± 0.5	2.7 ± 0.1	2.6 ± 0.5	2.2 ± 0.6
	14	10.4 ± 0.8	22.1 ± 1.2	50.6 ± 2.3	8.7 ± 0.9	6.9 ± 0.4	1.8 ± 0.3		
S137	3	23.3 ± 0.6	41.0 ± 1.8	25.4 ± 1.4	4.3 ± 0.8	3.3 ± 0.5	1.7 ± 0.2	1.4 ± 0.3	1.3 ± 0.3
	14	21.2 ± 1.3	42.7 ± 1.3	25.3 ± 2.1	5.7 ± 0.7	4.5 ± 0.8	1.1 ± 0.4		
S96	3	16.0 ± 0.9	40.7 ± 2.6	32.3 ± 1.2	5.3 ± 0.8	4.5 ± 0.7	1.9 ± 0.2	4.9 ± 0.6	3.3 ± 0.5
	14	11.4 ± 0.83	42.9 ± 1.3	26.8 ± 2.3	10.2 ± 0.9	7.9 ± 0.7	0.7 ± 0.3		
S67	3	11.4 ± 0.98	29.8 ± 1.5	42.6 ± 2.5	8.5 ± 0.8	5.7 ± 0.6	1.7 ± 0.2	6.3 ± 0.9	5.1 ± 0.7
	14	5.3 ± 0.6	30.6 ± 1.3	38.4 ± 2.6	14.8 ± 0.9	10.8 ± 0.9	0.2 ± 0.12		

with interrod spacing larger than 96 nm simultaneously inhibit these functions of cells compared to the corresponding 2D counterparts. As is known, the surface features of the material affecting the cell functions include chemistry,[3−6] surface energy/wettability,[3,7] roughness[8,9] and topography.[10−15] The NG, S67, S96, and S137 coatings involved in this work have the same surface chemistry (composed of Sr_1-HA) and a similar microscale roughness. The differences among the coatings are hydrophilicity and topography characterized by nanorod-shaped 3D patterns with similar diameter and aligned arrays of nanorods but different interrod spacing values relative to the nanogranulated 2D pattern. Surface hydrophilicity is believed to be an important factor in cell−material interactions, and studies have shown that hydrophilic surfaces induce osteoblastic cell growth and mineral deposition compared to hydrophobic surfaces.[3,8] Our results reveal that the S67 coating can significantly enhance cell proliferation and differentiation compared to the S96 coating, although both of the coatings have similar hydrophilicity, as characterized by the contact angles of the water droplets; furthermore, the S137 coating is more hydrophilic compared to the NG coating, whereas enhancements in the cell functions on the S137 coating are weaker than those on the NG coating. It is suggested that interrod spacing rather than hydrophilicity, in the present case, is the key factor affecting cell functions.

Intracellular Ca^{2+} signaling plays a key role in many aspects of osteoblast, which induces osteoblast proliferation by activation of the CaMKII and c-fos expressions as well as promotes osteoblast differentiation by activation of the fra-2 expression.[40] Figure 7 shows the Ca^{2+} concentrations in hFOB1.19 cells cultured on the coatings, which were measured using calcium assay kits, a method adopted and proven to be available by Xu et al.[41] At 3, 7, and 14 days, the intracellular Ca^{2+} concentrations are significantly up-regulated by the S67 and S96 coatings (especially S67) but down-regulated by the S137 coating compared to the NG coating, indicating that the nanorod-shaped 3D pattern can independently regulate the intracellular Ca^{2+} concentration by means of varying the interrod spacing relative to the nanogranulated 2D pattern. Recent works showed that greater intracellular Ca^{2+} concentration enhanced the proliferation and differentiation of mesenchymal stem cells;[42,43] therefore, the difference in the proliferation and differentiation of the osteoblasts on the nanorod-shaped 3D patterns can be well understood in terms of their interrod spacing values. However, the detailed mechanism needs further investigation.

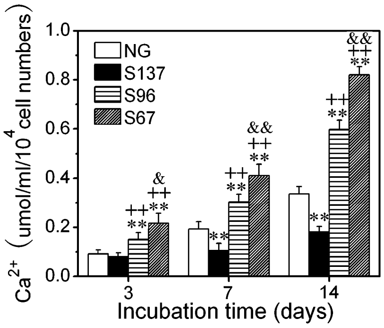

Figure 7. Ca^{2+} concentrations in osteoblasts cultured on the NG, S137, S96, and S67 coatings for 3, 7, and 14 days. Data are presented as the mean ± SD, $n = 4$, (**) $p < 0.01$ compared with the NG coating, (++) $p < 0.01$ compared with the S137 coating, and (&) $p < 0.05$ and (&&) $p < 0.01$ compared with the S96 coating.

4. CONCLUSION

Sr_1-HA nanorods with different interrod spacing values (67.3 ± 3.8, 95.7 ± 4.2, and 136.8 ± 8.7 nm) and nanogranulates were formed on microarc-oxidized microporous TiO_2 by a two-step method of MAO and HT and a one-step method of MAO, respectively, to form multilayer coatings. The coatings reveal two kinds of micro/nanoscaled hierarchical surfaces with a similar microscale roughness, e.g., a nanogranulated 2D pattern and a nanorod-shaped 3D pattern in nanotopography. The proliferation, differentiation, and biomineralization of osteoblasts can be regulated by the interrod spacing of the Sr_1-HA nanorods, which are significantly enhanced on the nanorod-shaped 3D patterns with interrod spacing smaller than 96 nm and more pronounced with decreasing interrod spacing but inhibited on the nanorods with spacing larger than 96 nm compared to the nanogranulated 2D pattern. Our study reveals the synergistic role played by the interrod spacing of 3D Sr_1-HA nanorods on osteoblast functions and provides insight into the surface structural design of a biomedical implant favoring osteointegration.

■ AUTHOR INFORMATION

Corresponding Author

*E-mail: yonghan@mail.xjtu.edu.cn. Tel.: +86 02982665580. Fax: +86 02982663453.

Notes

The authors declare no competing financial interest.

■ ACKNOWLEDGMENTS

We appreciate the National Program on Key Basic Research Project (973 Program) of China (Grant 2012CB619103) and National Natural Science Foundation of China (Grant 51071120) for financially supporting this work.

■ REFERENCES

(1) Divya, R. V. V.; Vinoth-Kumar, L.; Anitha, V. C.; Manzoor, K.; Deepthy, M.; Shantikumar, V. N. *Acta Biomater.* **2012**, No. 8, 1976−1989.

(2) Zhang, L.; Webster, T. J. *Nano Today* **2009**, *4*, 66−80.

(3) Liu, X. M.; Lim, J. Y.; Donahue, H. J.; Dhurjati, R.; Mastro, A. M.; Vogler, E. A. *Biomaterials* **2007**, *28*, 4535−4550.

(4) Heydarkhan-Hagvall, S.; Gluck, J. M.; Delman, C.; Jung, M.; Ehsani, N.; Full, S.; Shemin, R. J. *Biomaterials* **2012**, *33*, 2032−2040.

(5) Miron, R. J.; Oates, C. J.; Molenberg, A.; Dard, M.; Hamilton, D. W. T. *Biomaterials* **2010**, *31*, 449−460.

(6) Sugita, Y.; Ishizaki, K.; Iwasa, F.; Ueno, T.; Minamikawa, H.; Yamada, M.; Suzuki, T.; Ogawa, T. *Biomaterials* **2011**, *32*, 8374−8384.

(7) Lim, J. Y.; Shaughnessy, M. C.; Zhou, Z.; Noh, H.; Vogler, E. A.; Donahue, H. J. *Biomaterials* **2008**, *29*, 1776−1784.

(8) Setzer, B.; Bachle, M.; Metzger, M. C.; Kohal, R. J. *Biomaterials* **2009**, *30*, 979−990.

(9) Dolatshahi-Pirouz, A.; Jensen, T.; Kraft, D. C.; Foss, M.; Kingshott, P.; Hansen, J. L.; Larsen, A. N.; Chevallier, J.; Besenbacher, F. *ACS Nano* **2010**, *4*, 2874−2882.

(10) Zhao, L. Z.; Hu, L. S.; Huo, K. F.; Zhang, Y. M.; Wu, Z. F.; Chu, P. K. *Biomaterials* **2010**, *31*, 8341−8349.

(11) Okada, S.; Ito, H.; Nagai, A.; Komotori, J.; Imai, H. *Acta Biomater.* **2010**, *6*, 591−597.

(12) Kuo, S. W.; Lin, H. I.; Ho, J. H. C.; Shih, Y. R. V.; Chen, H. F.; Yen, T. J.; Lee, O. K. *Biomaterials* **2012**, *33*, 5013−5022.

(13) Liu, J.; Wang, X. D.; Jin, Q. M.; Jin, T. C.; Chang, S.; Zhang, Z. C.; Czajka-Jakubowska, A.; Giannobile, W. V.; Nör, J. E.; Clarkson, B. H. *Biomaterials* **2012**, *30*, 5036−5046.
(14) Park, J. K.; Kim, Y. J.; Yeom, J.; Jeon, J. H.; Yi, G. C.; Je, J. H.; Hahn, S. K. *Adv. Mater.* **2010**, *22*, 4857−4861.
(15) Brammer, K. S.; Choi, C.; Frandsen, C. J.; Oh, S.; Jin, S. *Acta Biomater.* **2011**, *7*, 683−690.
(16) Gupta, D.; Venugopal, J.; Mitra, S.; Dev, V. R. G.; Ramakrishna, S. *Biomaterials* **2009**, *30*, 2085−2094.
(17) Jang, J. H.; Castano, O.; Kim, H. W. *Adv. Drug Delivery Rev.* **2009**, *61*, 1065−1083.
(18) Guo, D. G.; Xu, K. W.; Han, Y. *J. Biomed. Mater. Res. A* **2008**, *86*, 947−958.
(19) Li, Y. F.; Li, Q.; Zhu, S. S.; Luo, E.; Li, J. H.; Feng, G.; Liao, Y. M.; Hu, J. *Biomaterials* **2010**, *31*, 9006−9014.
(20) Chen, H. F.; Tang, Z. Y.; Liu, J.; Sun, K.; Chang, S. R.; Peters, M. C.; Mansfield, J. F.; Czajka-Jakubowska, A.; Clarkson, B. H. *Adv. Mater.* **2006**, *18*, 1846−1851.
(21) Haders, D. J.; Burukhin, A.; Huang, Y. Z.; Cockayne, D. J. H.; Riman, R. E. *Cryst. Growth. Des.* **2009**, *9*, 3412−3422.
(22) Xiong, J. Y.; Li, Y. C.; Hodgson, P. D.; Wen, C. E. *Acta Biomater.* **2010**, *6*, 1584−1590.
(23) Ishizawa, H.; Ogino, M. *J. Biomed. Mater. Res.* **1995**, *29*, 1071−1079.
(24) Takebe, J.; Ito, S.; Champagne, C. M.; Cooper, L. F.; Ishibashi, K. *J. Biomed. Mater. Res. A* **2007**, *80*, 711−718.
(25) Song, H. J.; Shin, K. H.; Kook, M. S.; Oh, H. K.; Park, Y. J. *Surf. Coat. Technol.* **2010**, *204*, 2273−2278.
(26) Han, Y.; Sun, J. F.; Huang, X. *Electrochem. Commun.* **2008**, *10*, 510−513.
(27) Han, Y.; Chen, D. H.; Zhang, L. *Nanotechnology* **2008**, *19*, 335705.
(28) Han, Y.; Zhou, J. H.; Zhang, L.; Xu, K. W. *Nanotechnology* **2011**, *22*, 275603.
(29) Schiller, P. C.; D'Ippolito, G.; Balkan, W.; Roos, B. A.; Howard, G. A. *Bone* **2001**, *28*, 38−44.
(30) Civitelli, R. *Arch. Biochem. Biophys.* **2008**, *473*, 188−192.
(31) Owen, T. A.; Aronow, M.; Shalhoub, V.; Barone, L. M.; Wilming, L. M.; Tassinari, S.; Kennedy, M. B.; Pockwinse, S.; Lian, J. B.; Stein, G. S. *J. Cell Physiol.* **1990**, *143*, 420−430.
(32) Tsigkou, O.; Jones, J. R.; Polak, J. M.; Stevens, M. M. *Biomaterials* **2009**, *30*, 3542−3550.
(33) Komori, T. *J. Cell. Biochem.* **2006**, *99*, 1233−1239.
(34) Nakashima, K.; Zhou, X.; Kunkel, G.; Zhang, Z.; Deng, J. M.; Behringer, R. R.; Crombruqqhe, B. D. *Cell* **2002**, *108*, 17−29.
(35) Tsigkou, O.; Jones, J. R.; Polak, J. M.; Stevens, M. M. *Biomaterials* **2009**, *30*, 3542−3550.
(36) Viereck, V.; Siggelkow, H.; Tauber, S.; Raddatz, D.; Schutze, N.; Hufner, M. *J. Cell. Biochem.* **2002**, *8*, 348−356.
(37) Mizuno, M.; Fujisawa, R.; Kuboki, Y. *J. Cell. Physiol.* **2000**, *184*, 207−213.
(38) Ogawa, T.; Nishimura, I. *Int. J. Oral Maxillofac. Pathol.* **2003**, *18*, 200−210.
(39) Ogawa, T.; Sukotjo, C.; Nishimura, I. *J. Prosthodont.* **2002**, *11*, 241−247.
(40) Zayzafoon, M. *J. Cell. Biochem.* **2006**, *97*, 56−70.
(41) Xu, J. L.; Khor, K. A.; Sui, J. J.; Zhang, J. H.; Chen, W. N. *Biomaterials* **2009**, *30*, 5385−5391.
(42) Barradas, A. M.; Fernandes, H. A.; Groen, N.; Chai, Y. C.; Schrooten, J.; van de Peppel, J.; van Leeuwen, J. P.; van Blitterswijk, C. A.; de Boer, J. *Biomaterials* **2012**, *33*, 3205−3215.
(43) Liu, Y. K.; Lu, Q. Z.; Pei, R.; Ji, H. J.; Zhou, G. S.; Zhao, X. L.; Tang, R. K.; Zhang, M. *Biomed. Mater.* **2009**, *4*, 025004.